A study of a flexible fiber model and its behavior in DNS of turbulent channel flow

Acta Mechanica manuscript No.
(will be inserted by the editor)

A study of a flexible fiber model and its behavior in DNS of turbulent channel flow

Jelena Andrić · Sam T. Fredriksson · Stefan B. Lindström · Srdjan Sasic · Håkan Nilsson

Received: date / Accepted: date

Abstract The dynamics of individual flexible fibers in a turbulent flow field have been analyzed, varying their initial position, density and length. A particle-level fiber model has been integrated into a general-purpose, open source Computational Fluid Dynamics (CFD) code. The fibers are modeled as chains of cylindrical segments connected by ball and socket joints. The equations of motion of the fibers contain the inertia of the segments, the contributions from hydrodynamic forces and torques, and the connectivity forces at the joints. Direct Numerical Simulation (DNS) of the incompressible Navier–Stokes equations is used to describe the fluid flow in a plane channel and a one-way coupling is considered between the fibers and the fluid phase. We investigate the translational motion of fibers by considering the mean square displacement of their trajectories. We find that the fiber motion is primarily governed by velocity correlations of the flow fluctuations. In addition, we show that there is a clear tendency of the thread-like fibers to evolve into complex geometrical configurations in a turbulent flow field, in fashion similar to random conformations of polymer strands subjected to thermal fluctuations in a suspension. Finally, we show that fiber inertia has a significant impact on reorientation time-scales of fibers suspended in a turbulent flow field.

Keywords flexible fiber model · Direct Numerical Simulation (DNS) · CFD

J. Andrić, S. Sasic, H. Nilsson
Division of Fluid Dynamics, Department of Applied Mechanics, Chalmers University of Technology 412 96 Göteborg, Sweden
Tel.: +46-31-7721000
E-mail: jelena.andric@chalmers.se

S.T. Fredriksson
Department of Earth Sciences, University of Gothenburg, 405 30 Göteborg, Sweden

S.B. Lindström
Mechanics, Department of Management and Engineering, The Institute of Technology, Linköping University, 581 83 Linköping, Sweden

1 Introduction

The dynamics of particles suspended in flowing fluid are of high relevance in a great number of industrial processes. Particularly, suspensions of fibers and fiber flocs are processed to produce paper products and fiber composites. One example is the process of making pulp mats for use in hygiene products. When a fiber suspension is subjected to a flow field, the fibers may translate, rotate and deform. In the case of the production of fiber mats, these changes in the microstructures of the suspension affect the macroscopic properties of the produced material, such as elastic modulus, strength, and thermal and electric conductivities. In pulp and paper processing, the fiber dynamics of the sheet forming process are one of the most important factors that influence the sheet characteristics [23, 19].

To model these industrial processes, including wet forming of paper and dry forming of pulp mats, it is necessary to consider large particle systems in high Reynolds number flow with finite Reynolds number fiber–flow interactions [14]. The forming unit process in water-based papermaking has been previously modeled at a particle-level with direct numerical simulation (DNS) under a Stokes flow assumption [26] and with a microhydrodynamics approach for finite Reynolds numbers [16, 17]. The characteristics of dry forming, with large flow geometries and fibers suspended in air, present numerically more challenging conditions, since air is less dissipative than water and the time-resolution required to resolve undamped mechanical vibrations becomes a major obstacle. This work constitutes a first step toward tackling such intrinsically very challenging flows, and thus considers the motion of isolated fibers in a turbulent flow. The goal of the paper is thus to propose and describe a method that aims at investigating numerically the properties of flexible fibers in a directly simulated turbulent flow field.

As for numerical studies, a number of approaches have been developed to study particle-laden flows. In the Eulerian–Eulerian approach the phases are treated as interpenetrating continua. The Lagrangian–Eulerian approach, on the other hand, treats particles as moving objects in a fluid medium. In the DNS approach, the particle geometries are resolved to a high level of detail, giving excellent predictive capability for fiber motion in suspension [22, 24], but at a relatively high computational cost. Marchioli et al. [18] studied rigid fibers in a channel with turbulent flow, specifically investigating near-wall phenomena, fiber alignment and aggregation. In the microhydrodynamics approach, many particles are combined into a multi-rigid-body system, as previously discussed in [4, 15, 9]. The most suitable fiber suspension flow model for any given problem must be chosen while considering the problem size, the required resolution and time-scales of the problem [9]. We investigate the motion of fibers in a flow geometry much greater than the fiber length with a relatively high Reynolds number. Consequently, a microhydrodynamics approach is preferred in this instance.

Several microhydrodynamics approaches have been previously developed to simulate flexible fiber motion in shear and sedimentation flows. Matsuoka and Yamamoto [19] developed a particle-level simulation technique to capture the dynamics of rigid and flexible fibers in a prescribed flow field. They represented a fiber by a number of spheres, lined up and connected to each neighboring

sphere. Ross and Klingenberg [23] proposed a similar model, but using a chain of rigid, prolate spheroids. These numerical studies were in qualitative agreement with experimental results of isolated fiber motion obtained by Forgacs and Mason [7,8] and also predicted some of the rheological properties of fiber suspensions. Schmid et al. [25] developed a particle-level simulation technique to study flocculation of fibers in sheared suspensions in three dimensions. They investigated the influence of the shear rate, fiber shape, fiber flexibility, and frictional inter-particle forces on flocculation. The fibers were modeled as chains of massless, rigid, cylindrical segments interacting with an imposed flow field through viscous drag forces and with other fibers through contact forces. Lindström and Uesaka [15] further developed the model of Schmid et al. [25], by taking into account the particle inertia and the intermediate to long-range hydrodynamic interactions between the fibers. They derived an approximation of the non-creeping interaction between fiber segments and the surrounding fluid, for larger segment Reynolds numbers, and took into account the two-way coupling between the particles and the carrying fluid. Their simulations successfully reproduced the different regimes of motion for threadlike particles [15], and were subsequently used to study paper forming [16,17].

In the present paper, we are interested in the dynamics of individual flexible fibers suspended in a turbulent flow field. For that purpose, the flexible fiber model developed by Lindström and Uesaka [15] has been implemented in the OpenFOAM open source CFD software [28]. The aim is to have a detailed resolution of the flow field of the carrier phase in order to study fiber–flow interactions at intermediate to large Reynolds numbers, as motivated by the flow conditions of industrial forming processes. Particularly, we study the trajectories and reorientation of isolated, flexible fibers and how this depends on the initial fiber position, density and length.

2 Fiber model

In this section we describe the fiber geometry and its governing equations. Numerical algorithms to solve these equations are discussed as well. The present model does not include fiber-fiber interactions, i.e the fibers can cross each other.

2.1 Fiber geometry

Following the work of Schmid et al. [25] and Lindström and Uesaka [15], a fiber is modeled as a chain of N rigid cylindrical segments (see Fig. 1). The segments are indexed $i \in [1, N]$ and their locations are specified with respect to a global Cartesian coordinate system Γ. The axes of this inertial frame are defined by the base vectors $\{\hat{\boldsymbol{e}}_1, \hat{\boldsymbol{e}}_2, \hat{\boldsymbol{e}}_3\}$ and the origin is denoted by O. A single fiber segment has a diameter d_i, a length l_i, a start point P_i, and a unit vector $\hat{\boldsymbol{z}}_i$, which is aligned with the segment. The position of each fiber segment's center of mass is thus $\boldsymbol{r}_i = \overrightarrow{OP_i} + l_i\hat{\boldsymbol{z}}_i/2$.

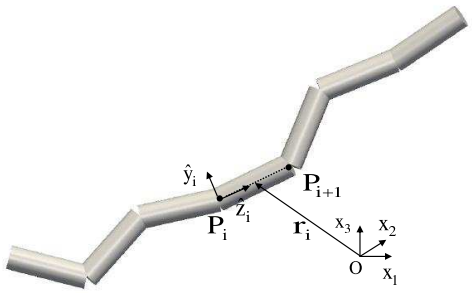

Fig. 1 Fiber geometry definitions.

2.2 Fiber equations of motion

The equations of motion comprise Euler's first and second law for each fiber segment i, as formulated in [25,15], yielding

$$m_i \ddot{\boldsymbol{r}}_i = \boldsymbol{F}_i^h + \boldsymbol{F}_i^w + \boldsymbol{X}_{i+1} - \boldsymbol{X}_i \tag{1a}$$

$$\frac{\partial(\boldsymbol{I}_i \cdot \boldsymbol{\omega}_i)}{\partial t} = \boldsymbol{T}_i^h + \frac{l_i}{2}\hat{\boldsymbol{z}}_i \times \boldsymbol{X}_{i+1} + \left(\frac{-l_i}{2}\hat{\boldsymbol{z}}_i\right) \times (-\boldsymbol{X}_i). \tag{1b}$$

In Eq. (1a), m_i is the mass of the segment, $\boldsymbol{F}_i^h$ is the hydrodynamic force acting on the segment i (see Sect. 2.3 and Appendix A), $\boldsymbol{F}_i^w$ is the sum of body forces, neglected in the present work, and $\boldsymbol{X}_i$ is the connectivity force exerted on segment $i-1$ by segment i. For the end segments $\boldsymbol{X}_1 = \boldsymbol{X}_{N+1} = \boldsymbol{0}$. In Eq. (1b), $\boldsymbol{I}_i$ is the tensor of inertia of segment i with respect to Γ, $\boldsymbol{\omega}_i$ is the angular velocity and $\boldsymbol{T}_i^h$ is the hydrodynamic torque (see Sect. 2.3). A fully flexible, thread-like fiber is considered, without any restoring moments in the ball and socket joints. The connectivity constraint between the fiber segments requires that the end-points of adjacent fiber segments coincide, *i.e.*

$$\boldsymbol{r}_i + \frac{l_i}{2}\hat{\boldsymbol{z}}_i = \boldsymbol{r}_{i+1} - \frac{l_{i+1}}{2}\hat{\boldsymbol{z}}_{i+1}. \tag{2}$$

The connectivity equation is then obtained by taking the time derivative of Eq. (2), yielding

$$\dot{\boldsymbol{r}}_{i+1} - \dot{\boldsymbol{r}}_i = \frac{l_i}{2}\boldsymbol{\omega}_i \times \hat{\boldsymbol{z}}_i + \frac{l_{i+1}}{2}\boldsymbol{\omega}_{i+1} \times \hat{\boldsymbol{z}}_{i+1}. \tag{3}$$

2.3 Hydrodynamic forces

The hydrodynamic forces and torques, $\boldsymbol{F}_i^h$ and $\boldsymbol{T}_i^h$, develop due to the velocity difference between the fiber segment and the fluid medium, as shown in detail in Appendix A. For a given velocity field $\boldsymbol{v}$ of the fluid, the strain-rate tensor is given as $\boldsymbol{G} = [\nabla \boldsymbol{v} + (\nabla \boldsymbol{v})^{\mathrm{T}}]/2$, with T denotes the transpose and $\boldsymbol{\Omega} = \nabla \times \boldsymbol{v}/2$

is the angular velocity of the fluid. The operators ∇ and $\nabla\times$ denote the gradient and the curl, respectively. The characteristic shear rate of the flow for fiber segment i is the $\dot{\gamma}_i = \sqrt{(1/2)(\boldsymbol{G}_i : \boldsymbol{G}_i)}$, where $\boldsymbol{G}_i$ is the local value of the strain rate tensor interpolated at position $\boldsymbol{r}_i$, and : is a double inner product. We define the segment Reynolds number as $\mathrm{Re}_s = \rho d \Delta v/\eta$, where ρ is the density of the fluid, η is its dynamic viscosity, d is the fiber diameter and Δv is the characteristic velocity difference between the fibers and the fluid. Here, we choose $\Delta v = l\dot{\gamma}$, where l is the segment length. The fiber diameter in wall units is 0.0068 and typically $\mathrm{Re}_s \approx 0.033$. The hydrodynamic forces are dominated by viscous effects at small segment Reynolds numbers $\mathrm{Re}_s \ll 1$, and by inertia effects for large segment Reynolds numbers $\mathrm{Re}_s \gg 1$. Lindström and Uesaka [15] numerically investigated the consequence of expressing viscous and inertia drag as a sum of two separable components, and found a fair agreement between the model, theory and experiments for a cylinder in cross-flow in the viscous flow regime ($\mathrm{Re}_s \lesssim 10^{-1}$) as well as in the regime dominated by dynamic effects ($10^2 \lesssim \mathrm{Re}_s \lesssim 3\times 10^5$). The maximum error in drag coefficient C_D is 42%, found in the intermediate interval of Reynolds numbers at $\mathrm{Re}_s \approx 5.4$. The total force and torque exerted on fiber segment i by the fluid are then given by

$$\boldsymbol{F}_i^h = \boldsymbol{F}_i^{h,v} + \boldsymbol{F}_i^{h,I} = (\boldsymbol{A}_i^v + \boldsymbol{A}_i^I)\cdot[\boldsymbol{v}(\boldsymbol{r}_i) - \dot{\boldsymbol{r}}_i] \tag{4a}$$

$$\boldsymbol{T}_i^h = \boldsymbol{T}_i^{h,v} + \boldsymbol{T}_i^{h,I} = (\boldsymbol{C}_i^v + \boldsymbol{C}_i^I)\cdot[\boldsymbol{\Omega}(\boldsymbol{r}_i) - \boldsymbol{\omega}_i] + (\boldsymbol{H}_i^v + \boldsymbol{H}_i^I) : \boldsymbol{G}(\boldsymbol{r}_i). \tag{4b}$$

Here, $\boldsymbol{A}_i^v$, $\boldsymbol{C}_i^v$, and $\boldsymbol{H}_i^v$ are the hydrodynamic resistance tensors of Stokes flow, $\boldsymbol{A}_i^I$, $\boldsymbol{C}_i^I$ and $\boldsymbol{H}_i^I$ are the dynamic resistance tensors, see Appendix A.

2.4 Discretized fiber equations of motion

The fiber equations of motion are discretized in time with a time step Δt. Subscripts $n-1$ and n denote the previous and the current time step, respectively. An implicit numerical scheme is used for calculating the segment velocity and angular velocity to enhance numerical stability. In all the equations presented in this section, the connectivity forces $\boldsymbol{X}_i$ and $\boldsymbol{X}_{i+1}$ are treated as unknowns. Using the expression for the hydrodynamic force (see Appendix A), Eq. (1a) can be discretized as

$$\frac{m}{\Delta t}(\dot{\boldsymbol{r}}_{i,n} - \dot{\boldsymbol{r}}_{i,n-1}) = \left(\boldsymbol{A}_{i,n-1}^v + \boldsymbol{A}_{i,n-1}^I\right)\cdot[\boldsymbol{v}\left(\boldsymbol{r}_{i,n-1}\right) - \dot{\boldsymbol{r}}_{i,n}] + \boldsymbol{X}_{i+1,n} - \boldsymbol{X}_{i,n}. \tag{5}$$

In the angular momentum equation (1b), the time differential term can be discretized as

$$\begin{aligned}\frac{\partial(\boldsymbol{I}_{i,n-1}\cdot\boldsymbol{\omega}_{i,n})}{\partial t} &= \dot{\boldsymbol{I}}_{i,n-1}\cdot\boldsymbol{\omega}_{i,n} + \boldsymbol{I}_{i,n-1}\cdot\dot{\boldsymbol{\omega}}_{i,n} \\ &\approx \dot{\boldsymbol{I}}_{i,n-1}\cdot\boldsymbol{\omega}_{i,n} + \frac{1}{\Delta t}\boldsymbol{I}_{i,n-1}\cdot(\boldsymbol{\omega}_{i,n} - \boldsymbol{\omega}_{i,n-1})\,.\end{aligned} \tag{6}$$

Using the expression for the hydrodynamic force (see Appendix A), Eq. (1b) yields

$$\begin{aligned}&\dot{\boldsymbol{I}}_{i,n-1}\cdot\boldsymbol{\omega}_{i,n}+\frac{1}{\Delta t}\boldsymbol{I}_{i,n-1}\cdot(\boldsymbol{\omega}_{i,n}-\boldsymbol{\omega}_{i,n-1})=(\boldsymbol{C}^{v}_{i,n-1}+\boldsymbol{C}^{I}_{i,n-1})\cdot\\&(\boldsymbol{\Omega}(\boldsymbol{r}_{i,n-1})-\boldsymbol{\omega}_{i,n})+(\boldsymbol{H}^{v}_{i,n-1}+\boldsymbol{H}^{I}_{i,n-1}):\boldsymbol{G}(\boldsymbol{r}_{i,n-1})\\&+\frac{l_i}{2}\hat{\boldsymbol{z}}_{i,n-1}\times(\boldsymbol{X}_{i+1,n}+\boldsymbol{X}_{i,n}).\end{aligned}\tag{7}$$

Finally, Eq. (3) is discretized as

$$\dot{\boldsymbol{r}}_{i+1,n}-\dot{\boldsymbol{r}}_{i,n}=\frac{l_i}{2}\boldsymbol{\omega}_{i,n}\times\hat{\boldsymbol{z}}_{i,n-1}+\frac{l_{i+1}}{2}\boldsymbol{\omega}_{i+1,n}\times\hat{\boldsymbol{z}}_{i+1,n-1}.\tag{8}$$

The momentum equation (5), the angular momentum equation (7) and the connectivity equation (8) form a system of equations, which can be solved for the unknown connectivity forces, velocities and angular velocities at time n. Since these variables have different physical units, the coefficients of the linear system will differ by many orders of magnitude and make the system ill-conditioned. Thus, a system of dimensionless equations should be considered.

2.5 Dimensionless connectivity force linear system

The dimensionless system of equations for the unknown connectivity forces, where $(*)$ denotes dimensionless quantities, reads

$$\boldsymbol{Q}^{*}_{i,n-1}\cdot\boldsymbol{X}^{*}_{i,n}+\boldsymbol{S}^{*}_{i,n-1}\cdot\boldsymbol{X}^{*}_{i+1,n}+\boldsymbol{T}^{*}_{i,n-1}\cdot\boldsymbol{X}^{*}_{i+2,n}=\boldsymbol{V}^{*}_{i,n-1}.\tag{9}$$

The corresponding dimensionless tensors are described in Appendix B. After applying Tikhonov regularization (see [1]), this system can be solved for the unknown dimensionless connectivity forces $\boldsymbol{X}^{*}_{i,n}$, $[2\leq i\leq N]$, while $\boldsymbol{X}^{*}_{1,n}=\boldsymbol{X}^{*}_{N+1,n}=\boldsymbol{0}$. In the present work, each fiber consists of $N=7$ segments so that the system takes the form

$$\begin{bmatrix}\boldsymbol{S}^{*}_{1,n-1}&\boldsymbol{T}^{*}_{1,n-1}&\boldsymbol{0}&\boldsymbol{0}&\boldsymbol{0}&\boldsymbol{0}\\\boldsymbol{Q}^{*}_{2,n-1}&\boldsymbol{S}^{*}_{2,n-1}&\boldsymbol{T}^{*}_{2,n-1}&\boldsymbol{0}&\boldsymbol{0}&\boldsymbol{0}\\\boldsymbol{0}&\boldsymbol{Q}^{*}_{3,n-1}&\boldsymbol{S}^{*}_{3,n-1}&\boldsymbol{T}^{*}_{3,n-1}&\boldsymbol{0}&\boldsymbol{0}\\\boldsymbol{0}&\boldsymbol{0}&\boldsymbol{Q}^{*}_{4,n-1}&\boldsymbol{S}^{*}_{4,n-1}&\boldsymbol{T}^{*}_{4,n-1}&\boldsymbol{0}\\\boldsymbol{0}&\boldsymbol{0}&\boldsymbol{0}&\boldsymbol{Q}^{*}_{5,n-1}&\boldsymbol{S}^{*}_{5,n-1}&\boldsymbol{T}^{*}_{5,n-1}\\\boldsymbol{0}&\boldsymbol{0}&\boldsymbol{0}&\boldsymbol{0}&\boldsymbol{Q}^{*}_{6,n-1}&\boldsymbol{S}^{*}_{6,n-1}\end{bmatrix}\cdot\begin{bmatrix}\boldsymbol{X}^{*}_{2,n}\\\boldsymbol{X}^{*}_{3,n}\\\boldsymbol{X}^{*}_{4,n}\\\boldsymbol{X}^{*}_{5,n}\\\boldsymbol{X}^{*}_{6,n}\\\boldsymbol{X}^{*}_{7,n}\end{bmatrix}=\begin{bmatrix}\boldsymbol{V}^{*}_{1,n-1}\\\boldsymbol{V}^{*}_{2,n-1}\\\boldsymbol{V}^{*}_{3,n-1}\\\boldsymbol{V}^{*}_{4,n-1}\\\boldsymbol{V}^{*}_{5,n-1}\\\boldsymbol{V}^{*}_{6,n-1}\end{bmatrix}.\tag{10}$$

After computing the dimensionless velocities and scaling them back to their dimensional form, new segment positions and orientations can be computed as

$$\boldsymbol{r}_{i,n}=\boldsymbol{r}_{i,n-1}+\Delta t\dot{\boldsymbol{r}}_{i,n}\tag{11}$$

$$\hat{\boldsymbol{z}}_{i,n}=\hat{\boldsymbol{z}}_{i,n-1}+\Delta t\,(\boldsymbol{\omega}_{i,n}\times\hat{\boldsymbol{z}}_{i,n-1}).\tag{12}$$

A correction of the segment positions is done at each time step to preclude the accumulation of errors. As in the algorithm implemented in [15], the middle fiber segment is fixed in space and all the other segments are translated to maintain the exact original fiber length.

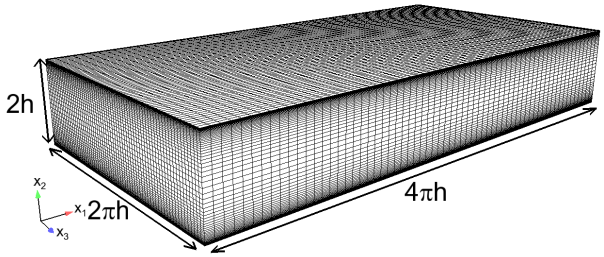

Fig. 2 Computational domain and coarse mesh. The fine mesh has three times more cells in the x_1 direction. The flow is in the x_1 direction. The boundary conditions in the x_1 and x_3 directions are cyclic and the boundary conditions in the x_2 direction are no-slip.

3 Fluid flow

The fibers are inserted into a fully developed turbulent flow field, computed using the Direct Numerical Simulation (DNS) technique. We describe the flow case, the numerical settings for the flow prediction, a validation of the resulting flow field, and a comparison between the results from two different mesh resolutions.

3.1 Flow case description

The turbulent flow in a plane channel is considered, and the results are validated with those of Davidson et al. [5]. The computational domain, and coarse mesh ($(64 \times 64 \times 64)$ cells) are illustrated in Fig. 2, while the fine mesh ($(192 \times 64 \times 64)$ cells) has three times more cells in in the x_1 direction. Both meshes are graded to resolve the near-wall gradients and flow structures. The first cell center is located at $x_2^+ = 0.33$. The flow configuration comprises a fully developed turbulent flow between two parallel smooth walls with no-slip conditions and unit normals $\pm\hat{\boldsymbol{e}}_2$. Cyclic boundary conditions are used in both x_1 and x_3 directions. The Navier–Stokes and continuity equations for incompressible flow are solved, *i.e.*

$$\frac{\partial \boldsymbol{v}}{\partial t} + \boldsymbol{v} \cdot \nabla \boldsymbol{v} = -\frac{1}{\rho}\nabla p + \frac{\eta}{\rho}\nabla^2 \boldsymbol{v} + E\hat{\boldsymbol{e}}_1 \tag{13}$$

$$\nabla \cdot \boldsymbol{v} = 0, \tag{14}$$

where $\boldsymbol{v}$ is the velocity, p is the pressure and E is the driving pressure gradient. The Reynolds number, $Re^* = \rho u^* h/\eta = 150$, is based on the friction velocity u^*, which relates to E and the channel half-width h.

The simulations are carried out using the OpenFOAM, open source CFD tool and a collocated finite volume approach. The time derivative is discretized using the second-order Crank-Nicholson scheme, and the convection term is discretized using the second-order central differencing scheme.

3.2 Flow validation

The present flow results are compared to the DNS results by Davidson et al. [5], which were in turn validated by DNS results by Kasagi and Iida [11]. Initial flow simulations are run, for each mesh resolution, until the flow is fully developed. The validation sampling is then done during 310 (coarse) and 203 (fine) through-flow cycles, using 50 (coarse) and 25 (fine) time realizations (samples). The velocities are first time-averaged and then also averaged spatially for each horizontal layer of cells. This yields the time-averaged velocity $\overline{\boldsymbol{U}} = \overline{U}(x_2)\hat{\boldsymbol{e}}_1$ as a function of x_2, shown in Fig. 3(a). A zoom of the near-wall region in log-log scale is shown in Fig. 3(b). The results from both meshes are identical, and very similar to DNS results in [5]. The mean velocity is then used in the calculation of the RMS values for each cell and finally the RMS values are spatially averaged for each horizontal layer. Figures 3(c) and 3(d) show the RMS velocity profile, of which the x_1 component decreases slightly while refining the mesh in the flow direction. The fine mesh reproduces the x_1 component of [5] completely.

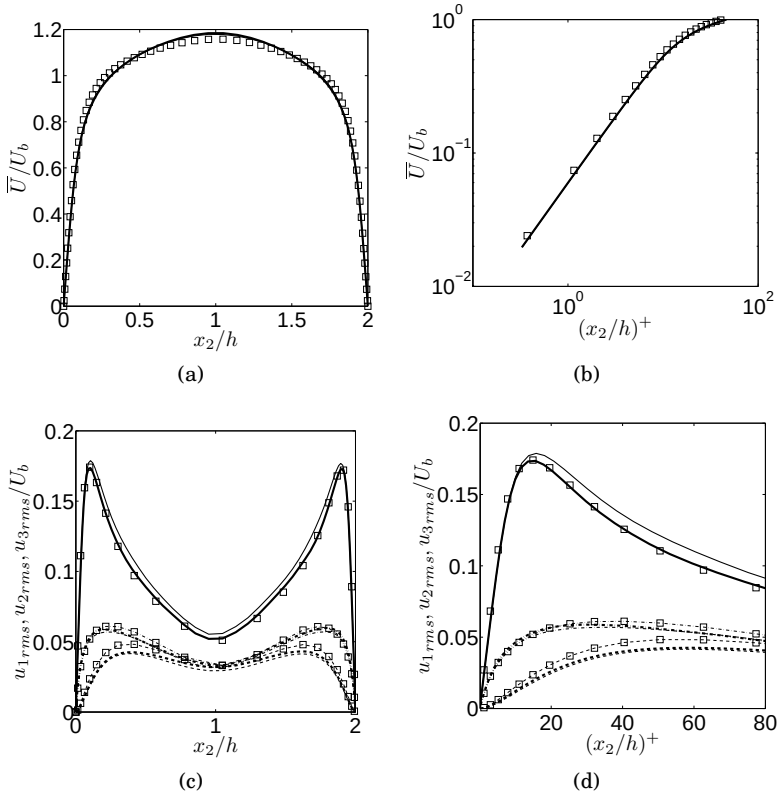

Fig. 3 Mean velocity and RMS velocity distributions. The thick and thin curves are the results of the present work for the fine mesh and coarse mesh, respectively. The results from Davidson et al. [5] are shown by square markers. (a) Mean flow velocities $\overline{\boldsymbol{U}}/\boldsymbol{U}_b$ for the full channel width (b) close to the wall. (c) RMS velocities for the full channel width. Solid curve: u_{1rms}/U_b, dashed curve: u_{2rms}/U_b, dash-dotted curve: u_{3rms}/U_b (d) close to the wall.

Being the important properties in fiber flow simulations, the mesh sensitivity of the mean and RMS vorticity is shown in Fig. 4, where $\nu = \eta/\rho$. Figures 4(a) and 4(b) show the mean vorticity as a function of x_2, and a zoom of the near-wall region. The results from the two mesh resolutions are identical. All components except the x_3 component are zero, which indicates that the averaging is sufficient. Figures 4(c) and 4(d) show the RMS vorticity as a function of x_2, and a zoom of the near-wall region. There is some mesh dependence in the RMS vorticity in the x_1 direction, while the other two components are much less dependent on the difference in resolution. Davidson et al. [5] did not provide such results, but the present results are very similar to those of Kim et al. [13], which were determined at a slightly different Reynolds number.

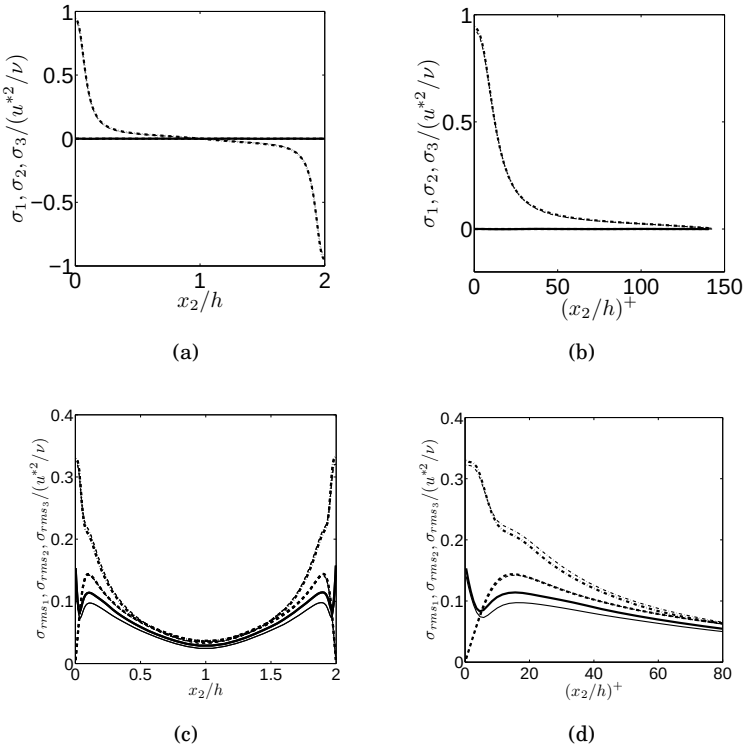

Fig. 4 Mean (a),(b) and RMS (c),(d) vorticity. The thick and thin curves are the results for the fine and coarse mesh respectively. Solid curve: x_1 component, dashed curve: x_2 component, dash-dotted curve: x_3 component (a) for the full channel width (b) close to the wall.

The comparisons show that the present results are very similar to the DNS results of Davidson et al. [5]. There is no mesh dependence for the mean quantities, but there is a small difference in the RMS of velocity and RMS of vorticity. The fine mesh simulation is chosen as a sufficiently good approximation of the flow for the current fiber simulation. Very similar results for the fiber behavior have been obtained for the coarse mesh, although not presented in the paper.

Table 1 Case specification

	Segment length	Segment density/Fluid density
Case1	$l = 0.02h$	1150
Case2	$l = 0.02h$	2300
Case3	$2/3\ l$	1150
Case4	$2/3\ l$	2300
Case5	$3/2\ l$	1150
Case6	$3/2\ l$	2300

4 Results and discussion

First, the simulation set-ups for different cases are described. In all the cases, the fibers are placed into the same flow field at the same time instance. The translational motion of the fibers and their reorientation are investigated.

4.1 Case descriptions

Six different cases were studied, in which the fiber segments' position, length and density were varied. The simulation time in viscous units is 81 for all the cases, and it is computed as a ratio between the actual time and the viscous time scale $t^+ = \nu/u^{*2}$. The simulation time corresponds to almost one through-flow simulation. The summary of the cases is given in Table 1. In each case, a total of 50 fibers are placed in the computational domain(see Fig. 5). The fibers are initially straight and vertical. Each fiber consists of seven segments (see Sect. 2.5). The segment response time is $\tau_s \approx m/(3\pi\eta l Y^A)$, which is the ratio between the fiber mass and the prefactor of the viscous component of the hydrodynamic resistance tensor and $\tau_s/t^+ \approx 13.5$. Neither fiber–fiber interactions nor two-way coupling is considered, so the fibers behave as if they were isolated.

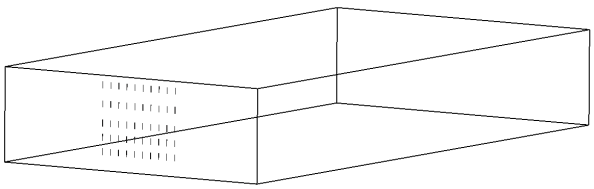

Fig. 5 Fiber at their initial positions in the computational domain.

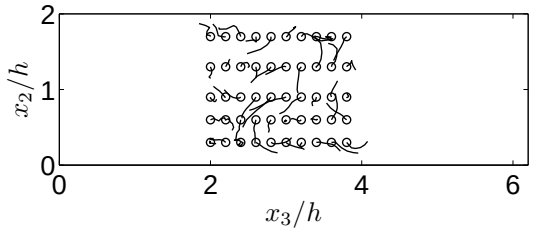

Fig. 6 The fiber trajectories projected to the x_3x_2 plane. The initial positions are shown by circles. The plotting box represents the channel cross-section.

4.2 Fiber translational motion

The trajectories $\boldsymbol{r}_G(t)$ of the centers of mass G of the fibers display apparent stochastic motion in the cross-directions due to the turbulence of the flow field (Fig. 6). In the absence of a flow perturbation, infinitesimal particle would trace the straight streamlines of $\overline{\boldsymbol{U}}$. However, for any finite turbulence $\widetilde{\boldsymbol{v}}$, particles will describe erratic, seemingly stochastic paths due to the apparent randomness of the fluctuating velocity field. At short time-scales, when the velocity fluctuations of the flow are still correlated, the particle is expected to move directionally with the flow, while at long time-scales, when the velocity fluctuations become de-correlated, diffusive-like motion is expected. For turbulent flows with an inertial sub-range, this de-correlation coincides with the Lagrangian integral time scale T_L. However, if the integral time scale is not clearly separated from the Kolmogorov microscale τ_η, the time-scale of transition into the diffusive regime is not trivially predicted, due to possible interference between these scales. For the present flow, the ratio between T_L and τ_η is small, indicating that there is no clear separation of scales and no distinct inertial sub-range, motivating further research.

The long time-scale stochastic quality of the particle trajectories has been previously described as a diffusion-like phenomenon, governed by the Fokker–Planck equation for translational motion [6]

$$\frac{\partial \Psi}{\partial t} - D_\mathrm{t}\nabla^2\Psi + \nabla\cdot(\overline{\boldsymbol{U}}\Psi) = 0, \tag{15}$$

where $\Psi(\boldsymbol{x},t)$ is the probability distribution function and D_t is the translational dispersion coefficient. The Fokker–Planck equation is valid for inertialess, Brownian particles. An approximate expression for the translational dispersion coefficient was derived assuming inertialess, rigid fibers in a homogeneous, isotropic turbulent flow [21], and diffusive-like behavior has been observed in simulations under those conditions, in the long time-scale limit [20].

It is of great interest and importance to investigate when the Fokker–Planck equation could be applied to turbulence-induced particle motion in a channel at time-scales relevant to industrial applications, such as papermaking.

For the particular flow geometry under study, $\overline{U}$ vanishes in the cross-direction of the channel, rendering

$$\frac{\partial \Psi}{\partial t} - D_\mathrm{t} \nabla^2 \Psi + \overline{U}(x_2) \frac{\partial \Psi}{\partial x_1} = 0. \tag{16}$$

Now, using the *ansatz* $\Psi(\boldsymbol{x}, t) = \Psi_1(x_1, t)\Psi_{23}(x_2, x_3, t)$, we obtain

$$\Psi_{23}\left[\frac{\partial \Psi_1}{\partial t} - D_\mathrm{t}\frac{\partial^2 \Psi_1}{\partial^2 x_1} + \overline{U}\frac{\partial \Psi_1}{\partial x_1}\right] + \Psi_1\left[\frac{\partial \Psi_{23}}{\partial t} - D_\mathrm{t}\left(\frac{\partial^2}{\partial^2 x_2} + \frac{\partial^2}{\partial^2 x_3}\right)\Psi_{23}\right] = 0.$$

A solution is obtained by requiring that each one of the two terms is zero. Consequently,

$$\frac{\partial \Psi_{23}}{\partial t} - D_\mathrm{t}\left(\frac{\partial^2}{\partial^2 x_2} + \frac{\partial^2}{\partial^2 x_3}\right)\Psi_{23} = 0. \tag{17}$$

If the origin is placed at the initial position of a particle, $\Psi_{23}(x_2, x_3, 0) = \delta(x_2, x_3)$, with δ the two-dimensional Dirac delta function, the solution of Eq. (17) becomes

$$\Psi_{23}(x_2, x_3, t) = \Psi_{23}(\rho, t) = \frac{\rho}{2D_\mathrm{t}t}\exp\left(-\frac{\rho^2}{4D_\mathrm{t}t}\right), \quad \rho = \sqrt{x_2^2 + x_3^2}. \tag{18}$$

The definition of the two-dimensional mean square displacement (MSD) yields

$$\mathrm{MSD}_{23}(t) = \int_0^\infty \rho^2 \Psi_{23}(\rho, t) d\rho = 4D_\mathrm{t}t, \quad t \geq 0, \tag{19}$$

which is a well-known result for Brownian motion in the plane [2].

For individual fiber trajectories $\boldsymbol{r}_G(t)$, the two-dimensional MSD is defined as

$$\mathrm{MSD}_{23}(t) = \int_{-\infty}^{\infty} \left|(\boldsymbol{\delta} - \hat{\boldsymbol{x}}_1\hat{\boldsymbol{x}}_1)\left[\boldsymbol{r}_G(\tau + t) - \boldsymbol{r}_G(\tau)\right]\right|^2 d\tau, \quad t \geq 0, \tag{20}$$

for which an estimate may be computed using the ensemble average of several particles studied for a finite time.

We compute $\mathrm{MSD}_{23}(t)$ from the observed particles trajectories (Fig. 7a), as well as the corresponding ensemble average MSD (Fig. 7b). It is obvious from the individual particle MSDs that they are superlinear in time. The ensemble average MSD for Case1 has the slope 1.926 in a log-log diagram (Fig. 7b) confirming that the fibers are strongly superdiffusive for the range of time-scales investigated. The MSD slope of ≈ 1.9 was observed in the remaining five cases as well. Importantly, since the Fokker–Planck equation infers that $\mathrm{MSD}_{23}(t) \propto t$ (see Eq. (20)), the observation that $\mathrm{MSD}_{23}(t) \propto t^{1.9}$ shows that the turbulent flow field does not exhibit diffusive-like fiber motion in the present case at the investigated time-scales, and that the Fokker–Planck equation does not describe the fiber motion at these time-scales. However, it is likely that there exists a regime of diffusive-like behavior at longer time-scales $t \gg T_L$, but the transition may be postponed, as previously mentioned, because this flow has no well-defined inertial sub-range. In many applications—papermaking, dry forming *etc.*—where the geometry is not extremely elongated, our results show that

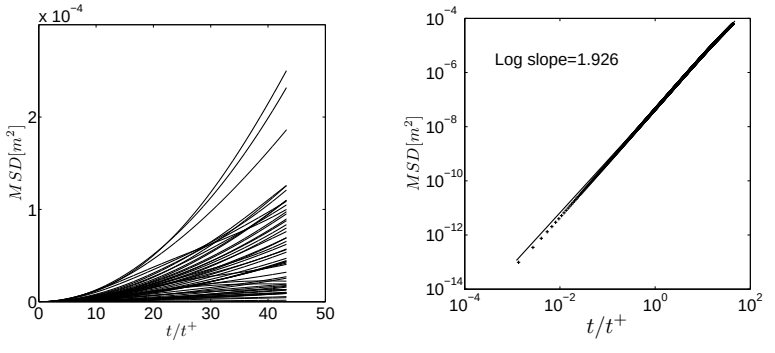

(a) (b)

Fig. 7 Case1. (a) MSD of individual particle trajectories. (b) Ensemble average of the MSD.

great caution must be taken in employing the Fokker–Planck equation to model the translational motion of fibers.

In this discussion, it is also important to say something in relation to the type of the processes governing the fluid dynamics and the motion of the particles. For example, when a diffusive regime is reached at longer time scales, the behavior of the underlying process depends exclusively on two mean quantities, namely its variance and its integral time scale. In other words, the behavior does not depend on the particular form of the autocorrelation of the process. However, for shorter time spans, the form of the autocorrelation plays a crucial role. Therefore, it is necessary for our analysis to specify that the process under study is statistically stationary, so that its autocorrelation function only depends on the time increment and not, for instance, on the starting time for the analysis. For such a process, the autocorrelation is parameterized by the integral time scale and becomes an exponential function of the time increment. Looking at the dispersion of fibers in a turbulent flow field, we also take the autocorrelation function of the fibers to be of the same type as that of the fluid, for example, the Lagrangian velocity autocorrelation function. In such a case, the integral time scale is to be modified due to the fact that the fibers have finite inertia, while the form of the function remains the same. Therefore, the conclusions presented above are fully valid for fibers suspended in an isotropic, stationary, turbulent flow field. Similar conclusions can be drawn for cases such as homogeneous turbulence with a constant velocity mean gradient (shear flows). However, for any other type of turbulence, very little can be said since any statistics is conditioned on location, prohibiting the *a priori* prediction of the form of the Lagrangian autocorrelation function. In this work we deal with a statistically stationary process and for that reason, we are able to clearly demarcate the particular results for long- and short-term processes, respectively.

It is observed that $\mathrm{MSD}_{23}(t) \propto t^{1.926}$ (Fig. 7b). This square dependence is consistent with the ballistic regime of particle motion. The ballistic regime is limited above by the fiber relaxation time τ_f, which is equal to the fiber segment relaxation time if one-way coupling is considered, and $\tau_f/t^+ = 13.5$. The MSD is also consistent with the directional push of the velocity fluctuations, which persist to a time-scale T_L. For the present flow, $T_L \gg \tau_f$, indicating that the

superdiffusive behavior is mainly explained by the velocity field, and not the inertia of the fibers.

4.3 Fiber reorientation

The reorientation of the initially vertical fibers has been studied. The orientation of a fiber with N segments is defined by

$$\hat{\boldsymbol{z}} = \frac{\boldsymbol{z}}{|\boldsymbol{z}|}, \quad \boldsymbol{z} = \sum_{i=1}^{N} \hat{\boldsymbol{z}}_i.$$

We quantify the alignment of the fiber with the flow direction by

$$z_1 = \hat{\boldsymbol{z}} \cdot \hat{\boldsymbol{e}}_1, \quad -1 \leq z_1 \leq 1.$$

and typically use $|z_1|$ to quantify orientation to account for the ambiguity in the enumeration of fiber segments. Moreover, the variance of the orientation is defined as

$$\sigma^2_{\hat{\boldsymbol{z}}} = \frac{1}{N-1} \sum_{i=1}^{N} |\hat{\boldsymbol{z}}_i - \hat{\boldsymbol{z}}|^2.$$

This variance is zero for straight fibers and increases as the fiber shape becomes coiled.

We consider the ensemble average for $|z_1|$ for the fibers initially positioned at different distances from the walls. The ensemble average, as well as $|z_1| \pm \sigma_{z_1}$ of Case1 are plotted in Fig. 8. There are two characteristic time-scales that can be observed. First, the time-scale ~ 13 of the initial ramp. This process of alignment in the flow direction could be due to the gradient of the average flow field, or due to the randomization of the fiber orientation due to turbulence. We observe that the ramp rate of vertically aligned fibers is in the order of the shear rate as predicted by [10] for stiff fibers in a linear shear gradient (Fig. 8). Investigating the signed orientation z_1 (Fig.9(a)), it is observed that the vertical fibers rotate with the vorticity of the flow, which infers that their alignment is mainly governed by the average shear gradient . Secondly, there is a time-scale ≈ 40 that appears to be associated with a randomization of the orientation of individual fiber segments, as supported by the steady increase of the variance (Fig. 9(b)). This second time-scale is inconsistent with the dimensionless half-period of Jeffery orbits for stiff fibers $(\pi(r_e + 1/r_e)/\dot{\gamma})/t^+ \approx 3378$, with r_e the equivalent aspect ratio of the fiber. The plot of the variance shows that the thread-like fibers evolve into increasingly complex geometrical conformations in a turbulent flow field, similarly to the random conformations of polymer strands subjected to thermal fluctuations in suspension. However, the simulation time is not sufficient for evaluating the steady-state characteristic size of these coils.

The influence of the fiber properties on their reorientation has also been investigated. From Fig. 10(a), it can be seen that the orientation change in the initial transient phase is slower for the heavier fibers. Notably, the heavier fibers have a longer relaxation time τ than those of base case. The initial ramp is thus dependent on the inertia of the particles. When the length of the fiber segment is varied in Fig. 10(b), no significant effect is observed on the fiber motion. This is

explained by the fact that the segment relaxation time is essentially unchanging when the segment length is varied, and this underscores the crucial role of the segment relaxation time for fiber motion in the investigated flow regime.

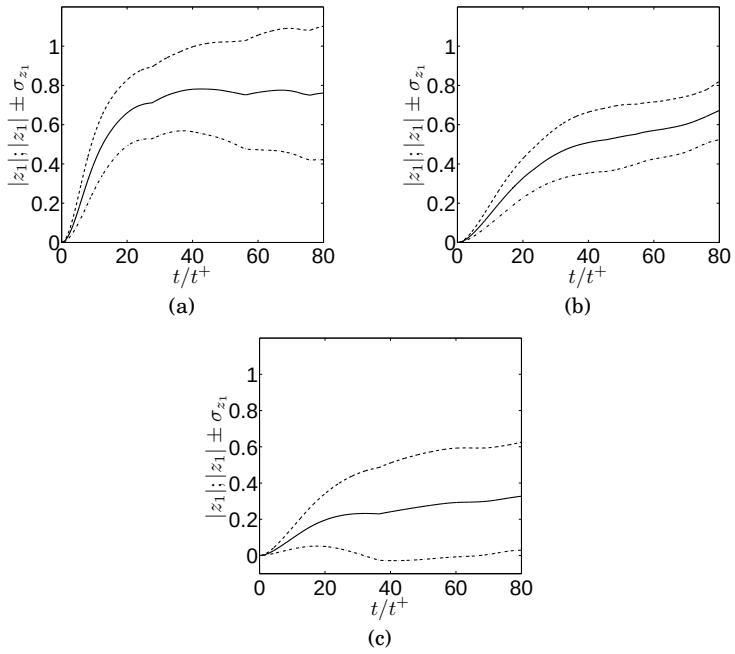

Fig. 8 Alignment of the fibers. Solid curve: ensemble average of $|z_1|$; dashed curve: $|z_1|$ + σ_{z_1}; dash-dotted curve:$|z_1|$ - σ_{z_1}. (a) Fibers initially closest to walls. (b) Fibers initially positioned in the next layers close to the walls. (c) Fibers initially positioned in the middle between the walls.

5 Conclusions

A particle-level flexible fiber model has been integrated into a general-purpose CFD code. The fibers are modeled as chains of cylindrical segments and their motion is described by Euler's first and second law for each segment. The fluid flow is described using DNS of the incompressible Navier–Stokes equations. The translational motion and reorientation of fibers suspended in a turbulent channel flow has been studied, with the parameters of the fibers and the fluid typical to those of cellulose fibers suspended in air. It was found that the fibers are superdiffusive at the investigated time-scales. The slope of the MSD is close to 2.0 when plotted in log-log scale. Because the relaxation times of the fibers are smaller than the Lagrangian integral time-scale, it is concluded that the superdiffusive regime is mainly governed by the flow fluctuations.

The reorientation of fibers in the turbulent field occurs at the time-scale of the reciprocal average shear rate for fibers aligned in the shear gradient direc-

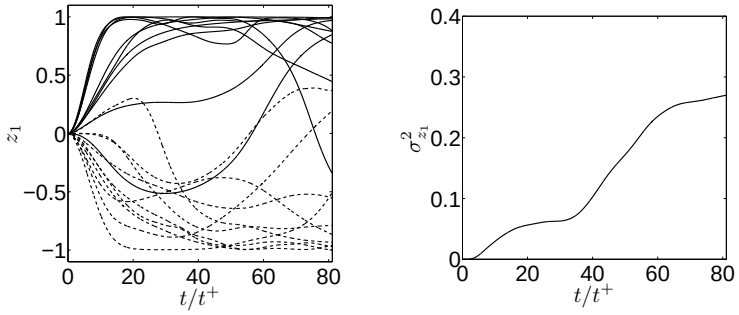

(a) (b)

Fig. 9 Orientational component z_1 for individual fibers. (a) Solid curve: initially closest to the lower wall; dashed curve: initially closest to the upper wall. (b) Variance

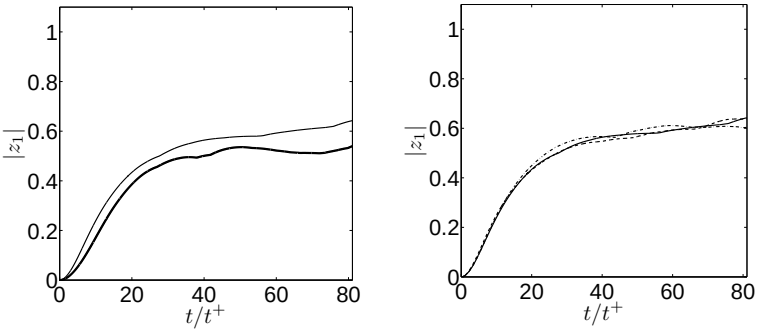

(a) (b)

Fig. 10 Alignment of fibers – dependence on segment length and density ratio. (a) Thin curve: lower segment density; thick curve: higher segment density. (b) Solid curve: segment length l; dashed curve: segment length $2/3l$; dash-dotted curve: segment length $3/2l$.

tion. This turbulence-induced reorientation should not be understood as alignment, but as a randomization of the orientation of individual segments; initially straight, thread-like particle reconform into coiled shapes in the turbulent field.

This investigation highlights several issues related to the flow of fibers suspended in air. For such a system, the ballistic regime ranges into relatively long time increments, and also, the fiber inertia affects the time-scales of fiber reorientation. From the point of application, the fiber-level dynamics of dry forming is dominated by inertia, contrasting the viscosity-dominated aqueous fiber suspensions typical to wet forming processes.

Acknowledgements The financial support from Bo Rydin Foundation and SCA Hygiene Products AB is greatly acknowledged. The Swedish National Infrastructure for Computing (SNIC) and Chalmers Centre for Computational Sciences and Engineering (C3SE) are acknowledged for providing computational resources.

A Viscous and dynamic drag forces

A.1 Viscous drag force

An analytical solution, described by [12], is available for the viscous drag force on an isolated spheroidal particle under laminar conditions. According to the semi-empirical formula of [3], a prolate spheroid is hydrodynamically equivalent to a finite circular cylinder in the sense that their orbiting behavior in shear flow is the same if

$$\frac{r_e}{r_c} = 1.24\,(\ln r_c)^{-1/2} \tag{21}$$

where r_e is the equivalent aspect ratio of the prolate spheroid and r_c is the cylinder aspect ratio. For fiber segment i with aspect ratio $r_c = l_i/d_i$, we choose the major axis of the hydrodynamically equivalent prolate spheroid to be $a_i = l_i$. Its minor axis, b_i is then obtained by inserting $r_e = a_i/b_i$ into Cox' formula:

$$b_i = \frac{1}{1.24} d_i \sqrt{\ln \frac{l_i}{d_i}} \tag{22}$$

Cox's formula is valid for isolated particles and a slender body approximation. None of these assumptions are true for fiber segments. However, [15] performed numerical experiments, which have shown that the error in the model predictions of orbit period of rigid fibers in shear flow becomes less than 3.4% compared to Eq. (21) for $r_c \geq 10$ when a two-way coupling is considered. Thus, the viscous drag force of a fiber segment is here approximated with that of a prolate spheroid, in accordance with [12]. For a given velocity field $\boldsymbol{v}$ of the fluid, the viscous hydrodynamic force $\boldsymbol{F}_i^{h,v}$ and torque $\boldsymbol{T}_i^{h,v}$ are defined by

$$\boldsymbol{F}_i^{h,v} = \boldsymbol{A}_i^v \cdot [\boldsymbol{v}(\boldsymbol{r}_i) - \dot{\boldsymbol{r}}_i] \tag{23}$$

$$\boldsymbol{T}_i^{h,v} = \boldsymbol{C}_i^v \cdot [\boldsymbol{\Omega}(\boldsymbol{r}_i) - \boldsymbol{\omega}_i] + \boldsymbol{H}_i^v : \boldsymbol{G}(\boldsymbol{r}_i) \tag{24}$$

The hydrodynamic resistance tensors $\boldsymbol{A}_i^v$, $\boldsymbol{C}_i^v$ and $\boldsymbol{H}_i^v$ are defined as

$$\boldsymbol{A}_i^v = 3\pi\eta l_i [Y_i^A \boldsymbol{\delta} + (X_i^A - Y_i^A)\hat{\boldsymbol{z}}_i\hat{\boldsymbol{z}}_i] \tag{25}$$

$$\boldsymbol{C}_i^v = \pi\eta l_i^3 [Y_i^C \boldsymbol{\delta} + (X_i^C - Y_i^C)\hat{\boldsymbol{z}}_i\hat{\boldsymbol{z}}_i] \tag{26}$$

$$\boldsymbol{H}_i^v = -\pi\eta l_i^3 Y_i^H (\boldsymbol{\epsilon} \cdot \hat{\boldsymbol{z}}_i)\hat{\boldsymbol{z}}_i, \tag{27}$$

where $\boldsymbol{\delta}$ and $\boldsymbol{\epsilon}$ are the unit and the permutation tensor, respectively. The parameters X_i^A, Y_i^A, X_i^C, Y_i^C and Y_i^H are the hydrodynamic coefficients, which depend on the eccentricity $e_i = \left(1 - b_i^2/a_i^2\right)^{1/2}$ and are defined as [12]

$$\begin{aligned}
L(e_i) &= \ln \frac{1+e_i}{1-e_i} \\
X_i^A(e_i) &= \frac{8}{3} e_i^3 [-2e_i + (1+e_i^2)L(e_i)]^{-1} \\
Y_i^A(e_i) &= \frac{16}{3} e_i^3 [2e_i + (3e_i^2 - 1)L(e_i)]^{-1} \\
X_i^C(e_i) &= \frac{4}{3} e_i^3 (1-e_i^2) [2e_i - (1-e_i^2)L(e_i)]^{-1} \\
Y_i^C(e_i) &= \frac{4}{3} e_i^3 (2-e_i^2) [-2e_i - (1+e_i^2)L(e_i)]^{-1} \\
Y_i^H(e_i) &= \frac{4}{3} e_i^5 [-2e_i + (1+e_i^2)L(e_i)]^{-1}.
\end{aligned} \tag{28}$$

A.2 Dynamic drag force

In the range $10^2 \lesssim Re_s \lesssim 3 \times 10^5$ of segment Reynolds numbers, the drag force of a cylinder in cross-flow is dominant as compared to the viscous drag in the axial direction. If $\hat{\boldsymbol{z}}_i$ is the cylinder orientation, then only the flow components in the plane perpendicular to $\hat{\boldsymbol{z}}_i$ need to be considered. The drag coefficient for cross flow over a circular cylinder is, according to [27], $C_D^I = 1$, for $10^2 \lesssim Re_s \lesssim 3 \times 10^5$. The total drag force and torque on a cylindrical fiber segment are obtained through integration over the infinitesimal cylinder slices. The dynamic drag force and torque are then given by

$$\boldsymbol{F}_i^{h,I} \approx \boldsymbol{A}_i^I \cdot [\boldsymbol{v}\left(\boldsymbol{r}_i\right) - \dot{\boldsymbol{r}}_i] \tag{29}$$

$$\boldsymbol{T}_i^{h,I} \approx \boldsymbol{C}_i^I \cdot [\boldsymbol{\Omega}\left(\boldsymbol{r}_i\right) - \boldsymbol{\omega}_i] + \boldsymbol{H}_i^I : \boldsymbol{G}\left(\boldsymbol{r}_i\right), \tag{30}$$

where the dynamic drag resistance tensors are

$$\begin{aligned} \boldsymbol{A}_i^I &= \frac{1}{2} C_D^I \rho d_i l_i v_{\perp,i} [\boldsymbol{\delta} - \hat{\boldsymbol{z}}_i \hat{\boldsymbol{z}}_i] \\ \boldsymbol{C}_i^I &= \frac{1}{24} C_D^I \rho d_i l_i^3 v_{\perp,i} [\boldsymbol{\delta} - \hat{\boldsymbol{z}}_i \hat{\boldsymbol{z}}_i] \\ \boldsymbol{H}_i^I &= \frac{1}{24} C_D^I \rho d_i l_i^3 v_{\perp,i} [(\boldsymbol{\epsilon} \cdot \hat{\boldsymbol{z}}_i)\, \hat{\boldsymbol{z}}_i] \end{aligned} \tag{31}$$

and $v_{\perp,i} = |\left(\boldsymbol{\delta} - \hat{\boldsymbol{z}}_i \hat{\boldsymbol{z}}_i\right) \cdot [\boldsymbol{v}(\boldsymbol{r}_i) - \dot{\boldsymbol{r}}_i]|$ is the cross-flow velocity of the fluid relative to the fiber segment.

B Dimensionless equations

The dimensionless tensors from the connectivity force linear system are given as

$$\boldsymbol{Q}^*_{i,n-1} = -(\frac{m^*}{\Delta t^*}\boldsymbol{\delta} + \boldsymbol{A}^{v*}_{i,n-1} + \boldsymbol{A}^{I*}_{i,n-1})^{-1} + \frac{3}{4r_p}\boldsymbol{C}^{*}_{\boldsymbol{z}\,i,n-1}$$

$$\boldsymbol{S}^*_{i,n-1} = (\frac{m^*}{\Delta t^*}\boldsymbol{\delta} + \boldsymbol{A}^{v*}_{i,n-1} + \boldsymbol{A}^{I*}_{i,n-1})^{-1} + (\frac{m^*}{\Delta t^*}\boldsymbol{\delta} + \boldsymbol{A}^{v*}_{i+1,n-1} + \boldsymbol{A}^{I*}_{i+1,n-1})^{-1}$$
$$+ \frac{3}{4r_p}\boldsymbol{C}^{*}_{\boldsymbol{z}\,i,n-1} + \frac{3}{4r_p}\boldsymbol{C}^{*}_{\boldsymbol{z}\,i+1,n-1}$$

$$\boldsymbol{T}^*_{i,n-1} = -(\frac{m^*}{\Delta t^*}\boldsymbol{\delta} + \boldsymbol{A}^{v*}_{i+1,n-1} + \boldsymbol{A}^{I*}_{i+1,n-1})^{-1} + \frac{3}{4r_p}\boldsymbol{C}^{*}_{\boldsymbol{z}\,i+1,n-1}$$

$$\boldsymbol{V}^*_{i,n-1} = -(\boldsymbol{s}^*_{i,n-1} - \boldsymbol{s}^*_{i+1,n-1} + r_p(\boldsymbol{b}^*_{i,n-1} + \boldsymbol{b}^*_{i+1,n-1}))$$

$$\boldsymbol{s}^*_{i,n-1} = (\frac{m^*}{\Delta t^*}\boldsymbol{\delta} + \boldsymbol{A}^{v*}_{i,n-1} + \boldsymbol{A}^{I*}_{i,n-1})^{-1} \cdot (\frac{m^*}{\Delta t^*}\dot{\boldsymbol{r}}^*_{i,n-1}$$
$$+ (\boldsymbol{A}^{v*}_{i,n-1} + \boldsymbol{A}^{I*}_{i,n-1}) \cdot \boldsymbol{v}^*(\boldsymbol{r}_{i,n-1}))$$

$$\boldsymbol{b}^*_{i,n-1} = \big((\boldsymbol{I}^*_{i,n-1} + \frac{1}{\Delta t^*}\boldsymbol{I}^*_{i,n-1} + \boldsymbol{C}^{v*}_{i,n-1} + \boldsymbol{C}^{I*}_{i,n-1})^{-1} \cdot (\frac{1}{\Delta t}\boldsymbol{I}^*_{i,n-1} \cdot \boldsymbol{\omega}^*_{i,n-1} +$$
$$(\boldsymbol{C}^{v*}_{i,n-1} + \boldsymbol{C}^{I*}_{i,n-1}) \cdot \boldsymbol{\Omega}^*(\boldsymbol{r}_{i,n-1}) + (\boldsymbol{H}^{v*}_{i,n-1} + \boldsymbol{H}^{I*}_{i,n-1}) : \boldsymbol{G}^*_{i,n-1}(\boldsymbol{r}_{i,n-1})\big) \times \hat{\boldsymbol{z}}_{i,n-1}$$

where $\boldsymbol{C}^{*}_{\boldsymbol{z}\,i,n-1}$ is a second-order tensor, which is a function of tensor $\left(\dot{\boldsymbol{I}}^*_{i,n-1} + \frac{1}{\Delta t^*}\boldsymbol{I}^*_{i,n-1} + \boldsymbol{C}^{v*}_{i,n-1} + \boldsymbol{C}^{I*}_{i,n-1}\right)^{-1}$ and the orientation vector $\hat{\boldsymbol{z}}_{i,n-1}$ and its components are

$C^*_{z\,i,n-1,11} = C^*_{I\,i,n-1,22}\hat{z}^2_{i,n-1,3} - C^*_{I\,i,n-1,23}\hat{z}_{i,n-1,2}\hat{z}_{i,n-1,3} - C^*_{I\,i,n-1,32}\hat{z}_{i,n-1,3}\hat{z}_{i,n-1,2}$
$+C^*_{I\,i,n-1,33}\hat{z}^2_{i,n-1,2}$

$C^*_{z\,i,n-1,12} = -C^*_{I\,i,n-1,21}\hat{z}^2_{i,n-1,3} + C^*_{I\,i,n-1,23}\hat{z}_{i,n-1,1}\hat{z}_{i,n-1,3} + C^*_{I\,i,n-1,31}\hat{z}_{i,n-1,2}$
$\hat{z}_{i,n-1,3} - C^*_{I\,i,n-1,33}\hat{z}_{i,n-1,1}\hat{z}_{i,n-1,2}$

$C^*_{z\,i,n-1,13} = C^*_{I\,i,n-1,21}\hat{z}_{i,n-1,2}\hat{z}_{i,n-1,3} - C^*_{I\,i,n-1,22}\hat{z}_{i,n-1,1}\hat{z}_{i,n-1,3} - C^*_{I\,i,n-1,31}\hat{z}^2_{i,n-1,2}$
$+C^*_{I\,i,n-1,32}\hat{z}_{i,n-1,1}\hat{z}_{i,n-1,2}$
$C^*_{z\,i,n-1,21} = C^*_{I\,i,n-1,32}\hat{z}_{i,n-1,3}\hat{z}_{i,n-1,1} - C^*_{I\,i,n-1,33}\hat{z}_{i,n-1,1}\hat{z}_{i,n-1,2} - C^*_{I\,i,n-1,12}\hat{z}^2_{i,n-1,3}$
$+C^*_{I\,i,n-1,13}\hat{z}_{i,n-1,2}\hat{z}_{i,n-1,3}$
$C^*_{z\,i,n-1,22} = -C^*_{I\,i,n-1,31}\hat{z}_{i,n-1,1}\hat{z}_{i,n-1,3} + C^*_{I\,i,n-1,33}\hat{z}^2_{i,n-1,1} + C^*_{I\,i,n-1,1}\hat{z}^2_{i,n-1,3}$
$-C^*_{I\,i,n-1,13}\hat{z}_{i,n-1,1}\hat{z}_{i,n-1,3}$
$C^*_{z\,i,n-1,23} = C^*_{I\,i,n-1,31}\hat{z}_{i,n-1,1}\hat{z}_{i,n-1,2} - C^*_{I\,i,n-1,32}\hat{z}^2_{i,n-1,1} - C^*_{I\,i,n-1,11}\hat{z}_{i,n-1,2}\hat{z}_{i,n-1,3}$
$+C^*_{I\,i,n-1,12}\hat{z}_{i,n-1,1}\hat{z}_{i,n-1,3}$
$C^*_{z\,i,n-1,31} = C^*_{I\,i,n-1,12}\hat{z}_{i,n-1,2}\hat{z}_{i,n-1,3} - C^*_{I\,i,n-1,13}\hat{z}^2_{i,n-1,2} - C^*_{I\,i,n-1,22}\hat{z}_{i,n-1,1}\hat{z}_{i,n-1,3}$
$+C^*_{I\,i,n-1,23}\hat{z}_{i,n-1,2}\hat{z}_{i,n-1,1}$
$C^*_{z\,i,n-1,32} = -C^*_{I\,i,n-1,11}\hat{z}_{i,n-1,2}\hat{z}_{i,n-1,3} + C^*_{I\,i,n-1,13}\hat{z}_{i,n-1,1}\hat{z}_{i,n-1,3} + C^*_{I\,i,n-1,21}\hat{z}_{i,n-1,3}$
$\hat{z}_{i,n-1,1} - C^*_{I\,i,n-1,23}\hat{z}^2_{i,n-1,1}$
$C^*_{z\,i,n-1,33} = C^*_{I\,i,n-1,11}\hat{z}_{i,n-1,2}\hat{z}_{i,n-1,3} - C^*_{I\,i,n-1,12}\hat{z}_{i,n-1,1}\hat{z}_{i,n-1,2} - C^*_{I\,i,n-1,21}\hat{z}_{i,n-1,2}$
$\hat{z}_{i,n-1,1} + C^*_{I\,i,n-1,22}\hat{z}^2_{i,n-1,1}$

References

1. J. Andrić, Implementation of a flexible fiber model in a general purpose CFD code. Thesis for Licentiate of Engineering no. 2012:04, Chalmers University of Technology, Göteborg, Sweden (2012)
2. S. Chandrasekhar, Stochastic problems in physics and astronomy, *Rev. Mod. Phys.*, 15:1-89 (1943)
3. R. G. Cox, The motion of long slender bodies in a viscous fluid. Part 2. Shear flow, *J. Fluid Mech.*, 45:625-657 (1971)
4. C. T. Crowe, M. Sommerfeld, and Y. Tsuji, *Multiphase Flows With Droplets and Particles*, CRC, New York (1998)
5. L. Davidson, D. Cuturic and S. H. Peng, DNS in a plane vertical channel with and without buoyancy, In *Turbulence, heat and mass transfer*, eds. K. Hanjalic, Y. Nagano, and M. J. Tummers, Vol. 4, 401-408 Begel House Inc., New York, Wallingford (UK) (2003)
6. M. Doi and S. Edwards, *The theory of polymer dynamics*, Oxford: Clarendon Press (1988)
7. O. L.Forgacs and S. G. Mason, Particle Motions in Sheared Suspensions: IX.Spin and deformation of threadlike particles, *Journal of Colloid Science*, 14: 457-472 (1959a)
8. O. L. Forgacs and S. G. Mason, Particle Motions in Sheared Suspensions: X.Orbits of flexible threadlike particles, *Journal of Colloid Science*, 14: 473-491 (1959b)
9. J. Hämäläinen, S.B. Lindström, T. Hämäläinen, and T. Niskanen, Papermaking fiber suspension flow simulations at multiple scales, *J. Eng. Math.*, 71(1): 55-79 (2011)
10. G. B.Jeffery, The motion of ellipsoidal particles immersed in a viscous fluid, *Proc. Roy. Soc. London Ser. A*, 102: 161-179 (1922)
11. N.Kasagi and O. Iida, Progress in direct numerical simulation of turbulent heat transfer. In *ASME/JSME Joint Thermal Engineering Conference*, San Diego, California (1999)
12. S. Kim and S. J. Karilla, *Microhydrodynamics: Principles and selected applications*, Butterworth-Heinemann, Stoneham (1991)
13. J. Kim, P. Moin and R. Moser, Turbulence statistics in fully developed channel flow at low Reynolds number turbulence in channel flow at low Reynolds number, *Journal of Fluid Mechanics*, 177: 133-166 (1987)
14. S. B. Lindström, Modeling and simulation of paper structure development. PhD diss, Mid Sweden University, Sundsvall, Sweden (2008)
15. S. B. Lindström and T. Uesaka, Simulation of the motion of flexible fibers in viscous fluid flow, *Physics of Fluids*, 19: 113307 (2007)
16. S. B. Lindström and T. Uesaka, Particle-level simulation of forming of the fiber network in papermaking, *Int. J. Eng. Sci.*, 46(9): 858-876 (2007)
17. S. B. Lindström, T.Uesaka and U.Hirn, Evolution of the paper structure along the length of a twin-wire former. In *14th Fund. Res. Symp.*, ed. S. J. I'Anson, Vol. 1, 207-245. Oxford, UK (2009)

18. C.Marchioli, M. Fantoni, and A. Soldati, Orientation, distribution, and deposition of elongated, inertial fibers in turbulent channel flow, *Phys. Fluids*, 22: 033301 (2010)
19. T. Matsuoka and S. Yamamoto, Dynamic simulation of fiber suspensions in shear flow, *J. Chem. Phys.*, 102: 2254 (1995)
20. J. A.Olson, The motion of fibres in turbulent flow, stochastic simulation of isotropic homogenous turbulence, *Int. J. Multiphase Flow*, 27: 2083-2103 (2001)
21. J. A.Olson and R. J. Kerekes, The motion of fibres in turbulent flow, *J. Fluid Mech.*, 377: 47-64 (1998)
22. D. Qi, Direct simulations of flexible cylindrical fiber suspensions in finite Reynolds number flows, *J. Chem. Phys.*, 125: 114901 (2006)
23. R. F. Ross and D.J. Klingenberg, Dynamic simulation of flexible fibers composed of linked rigid bodies, *J. Chem. Phys.*, 106: 2949-2960 (1997)
24. A. Salahuddin, J. Wu and C. K. Aidun, Numerical study of rotational diffusion in sheared semidilute fiber suspension, *J. Fluid Mech.*, 692: 153-182 (2012)
25. C. F. Schmid, L. H. Switzer and D. J. Klingenberg, Simulation of fiber flocculation: effects of fiber properties and interfiber friction, *J. Rheol.*, 44: 781-809 (2000)
26. E. Svenning, A. Mark, F. Edelvik, E. Glatt, S. Rief, A. Wiegmann, L. Martinsson, R. Lai, M. Fredlund and U. Nyman, Multiphase simulation of fiber suspension flows using immersed boundary methods, *Nordic Pulp Paper Res. J.*, 27: 184-191 (2012)
27. D. J.Tritton, *Physical fluid dynamics*, Clarendon, Oxford (1988)
28. H. Weller, G. Tabor, H. Jasak, and C. Fureby, A tensorial approach to computational continuum mechanics using object-oriented techniques, *Computers in physics*, 12(6): 620-631 (1998)